ELSEVIER

NeuroImage

www.elsevier.com/locate/ynimg
NeuroImage 32 (2006) 1060–1069

Shape differences of the brain ventricles in Alzheimer's disease

Luca Ferrarini,[a] Walter M. Palm,[b] Hans Olofsen,[a] Mark A. van Buchem,[b] Johan H.C. Reiber,[a] and Faiza Admiraal-Behloul[a,b,*]

[a]*Division of Image processing, Leiden University Medical Center, Leiden, The Netherlands*
[b]*Department of Radiology, Leiden University Medical Center, Leiden, The Netherlands*

Received 11 January 2006; revised 19 May 2006; accepted 23 May 2006
Available online 12 July 2006

The brain ventricles are surrounded by gray and white matter structures that are often affected in dementia in general and Alzheimer's disease (AD) in particular. Any change of volume or shape occurring in these structures must affect the volume and shape of the ventricles. It is well known that ventricular volume is significantly higher in AD patients compared to age-matched healthy subjects. However, the large overlap between the two volume distributions makes the measurement unsuitable as a biomarker of the disease. The purpose of this work was to assess whether local shape differences of the ventricles can be detected when comparing AD patients and controls. In this work, we captured the ventricle's shape and shape variations of 29 AD subjects and 25 age-matched controls, using a fully automatic shape modeling technique. By applying permutation tests on every single node of a mesh representation of the shapes, we identified local areas with significant differences. About 22% of an average surface of the ventricles presented significant difference ($P < 0.05$) (~14% of the left against ~7% of the right side). We found out that in patients with Alzheimer disease, not only the lateral horns were significantly affected, but also the areas adjacent to the anterior corpus callosum, the splenium of the corpus callosum, the amygdala, the thalamus, the tale of the caudate nuclei (especially the left one), and the head of the left caudate nucleus.

Introduction

Alzheimer's disease (AD) is the most common form of dementia in middle-aged and older adults. It is a progressive, irreversible, and degenerative brain disorder that causes impairment in memory, thinking, and behavior. The vast emotional and economic costs of this disease are continuously growing, as the population gets older. Although the risk of developing AD increases with age, AD is by no means a part of the normal aging process. In the absence of this disease, the human brain can often operate properly to the age of 100 and beyond.

The imaging-based measurements of disease progression in AD that have received the most attention are MRI measures of the rate of change in whole-brain volume and hippocampus volume (Freeborough and Fox, 1997; Nichols and Holmes, 2001; Pitiot et al., 2003; Rueckert et al., 2003; Scheltens et al., 1995; Schott et al., 2005; Thodberg, 2003). Early studies showed that the brain volume decreases and cerebrospinal fluid volume increases with advancing age. It has been shown in (Showell et al., 2003; Thompson et al., 2003) that different brain regions lose volume at different rates in a non-linear region-dependent manner, with prefrontal volume declining more rapidly than other brain regions (Coffey et al., 1992; Raz et al., 1997). Different diseases with different phenotypic presentations may be associated with specific patterns of regional atrophy. Studies in AD have shown prominent early involvement of medial temporal lobe structures, especially the entorhinal cortex and the hippocampus (Barns et al., 2004; Dekaban, 1978; Lerch et al., 2005; Pruessner et al., 2001).

In AD, there is increasing evidence of marked damage and dysfunction not only in the gray matter but also in the white matter (Armstrong et al., 2004; Bronge et al., 2002; Spilt et al., 2005). Neuropathological and biochemical studies on white matter from AD subjects have demonstrated dramatic loss of myelin and axons (Bronge et al., 2002; Scheltens et al., 1995). Several studies have demonstrated that structural white matter changes such as atrophy of the corpus callosum are significantly greater in AD than in healthy subjects (Bozzao et al., 2001; Hanyu et al., 1999; Teipel et al., 2002).

The brain ventricles (see Fig. 1) are in the center of the brain, surrounded by gray and white matter structures that are often affected by dementia diseases: deep white matter, corpus callosum, hippocampus, amygdala, caudate nucleus, and thalamus. All these structures are subject to atrophy in the presence of dementia. Any change of volume or shape occurring in these structures must affect the shape and volume of the ventricles.

It is well known that brain ventricle volume is significantly higher in AD patients compared to age-matched healthy subjects. However, the distributions of volume measurements of both groups

* Corresponding author. Department of Radiology, Leiden University Medical Center, Leiden, The Netherlands.
E-mail address: f.behloul@lumc.nl (F. Admiraal-Behloul).
Available online on ScienceDirect (www.sciencedirect.com).

1053-8119/$ - see front matter © 2006 Elsevier Inc. All rights reserved.
doi:10.1016/j.neuroimage.2006.05.048

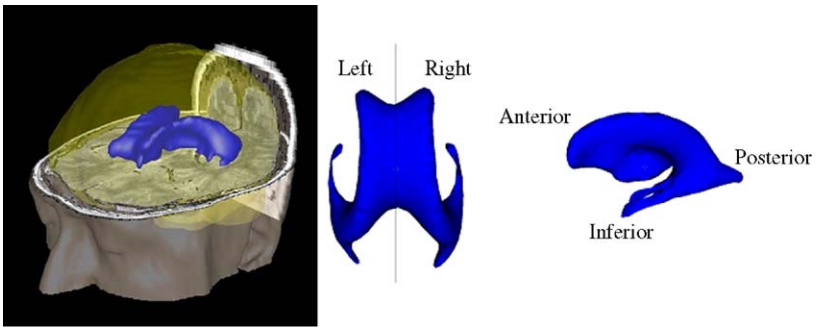

Fig. 1. The brain ventricles discussed in this paper follow the indications shown in this image: left, right, anterior, and posterior are considered from the patient's point of view.

present a large overlap, which makes the volume measurement not suitable as a biomarker.

The purpose of this work was first to study the shape of the brain ventricles and their variations in healthy elderly and AD subjects, and second to investigate the presence of significant shape differences between the two groups. The shape of brain ventricles is highly concave and therefore challenging to model and analyze: it requires therefore sophisticated computing techniques.

Methods

Subjects

Twenty-nine patients with probable AD (12 men, 17 women, mean age 73 years, age range 60–83 years) and 25 volunteers with normal cognitive function (11 men, 14 women, mean age 74 years, age range 64–89 years) were included. The patients with probable AD had been consecutively referred to our outpatient memory clinic. The volunteers had been recruited through an advertisement in a local newspaper. All subjects were evaluated for memory loss using a standardized dementia screening that included a detailed medical history, a general internal and neurological exam, laboratory tests, neuropsychological testing including the Mini Mental State Examination (MMSE), and magnetic resonance images (MRI) of the brain. Of the 29 patients with probable AD, 2 patients were severely demented (MMSE <10), 20 patients were moderately demented (9 < MMSE < 21), and 7 patients were mildly demented (MMSE >20). Diagnoses were made in a multidisciplinary consensus meeting according to the National Institute of Neurological and Communicative Disorders and Stroke-Alzheimer's Disease and Related Disorders Association (NINCDS-ADRDA) criteria for probable AD. Patients and controls were included if they (1) were older than 60 years, (2) had no other neurologic or psychiatric illness, and (3) had no abnormalities on MRI other than white matter hyperintensities or an incidental small lacunar lesion (≤5 mm diameter). The study was approved by the local Medical Ethical Committee. Written informed consent was obtained from all subjects or from a close relative if a patient was demented.

MRI acquisition and pre-processing

MRI was performed on a 1.5-T MR-system (Philips Medical Systems, Best, The Netherlands) using the following pulse sequences: dual fast spin-echo (proton density and T2 weighted): time to echo (TE) 27 ms, repetition time (TR) 3000 ms, 48 contiguous 3-mm slices without an interslice gap, matrix 256 × 256, field of view (FOV) 220 mm. FLAIR (fluid attenuated inversion recovery): TE 100 ms, TR 8000, 48 contiguous 3-mm slices without an interslice gap, matrix 256 × 256, FOV 220.

In-house developed automated segmentation software (SNIPER, Software for Neuro-Image Processing in Experimental Research) that combines template-based fuzzy clustering, fuzzy inference, and region-growing techniques was used to pre-process the images. Using the method described in Admiraal-Behloul et al. (2005), the software extracts fully automatically the intracranial cavity, the cerebrospinal fluids (CSF), and the white matter hyperintensities. The lateral and third ventricles were semi-automatically extracted by re-labeling the wrongly segmented ventricular CSF to ventricles; this was done using interactive editing tools: the user, by a simple click, re-labels pre-segmented CSF. The re-labeling has been done slice-by-slice, using 2D region growing.

For shape modeling and statistical comparison purposes, all the images were corrected for brain size and orientation by linear mapping into a stereotaxic space using an affine 12-parameter transformation (Woods et al., 1998). The LUMC T2-weighted brain template for geriatrics was used as target image for the automatic registration (Admiraal-Behloul et al., 2003).

Statistical shape modeling

The notion of biological shape seems reasonably well explained by a statistical description over a large population of instances (Cootes et al., 1995). The model building requires, as a key step, the establishing of correspondence between shape surfaces over a large set of training examples. Finding correspondence between two surfaces implies finding corresponding elements that share position and/or shape similarities. Finding the right way to define correspondent points on different shapes is difficult. In some 2D application, manual "landmark" definition might be possible, but it becomes unpractical when 3D shapes are considered due to the larger amount of data. In 3D, the manual landmark definition is time consuming, poorly reproducible, and error prone. The problem can be summarized in 3 main questions: "How many landmarks or nodes (in mesh representation) are needed?", "Where should they be located?", and "How can one define node correspondence across several instances of shapes?"

In a previous work (Ferrarini et al., 2005), we showed how to use growing neural networks to answer all three questions. Most of the growing neural networks are variations of the growing cell structure (GCS) introduced by Fritzke (1994). Marsland presented a Self-Organizing Network That Grows When Required (SONGWR) (Marsland et al., 2002). SONGWRs proved to be (1) more data-driven while growing and (2) faster in learning input representation when compared with previous models.

In a SONGWR, each node is associated with a subspace of the input space. The network is initialized with few nodes randomly located in the input space and not connected together. At each iteration, a new input is given to the network; in order to maintain a good representation of the input space, the existing nodes are moved or removed (adaptation), or new nodes and connections are added to the network (growing) (see Fig. 2). The process is repeated until convergence: a final model of the input space (at a desired accuracy level) is reached. The SONGWR principle is based on self-organizing maps (SOM) (Fritzke, 1992), which are known to be perfectly topology-preserving: the network preserves neighborhood relations in the data by mapping neighboring inputs onto neighboring nodes in the map.

In case of shape modeling, the input space of the neural network is the whole set of surface points extracted from the object to be modeled (i.e., extracted from segmented brain ventricles). A representative instance of the shape is used as input for the growing and adapting iterative algorithm. Once the SONGWR algorithm has converged, the optimal number of nodes and their spatial locations are identified. The next step is to find corresponding nodes across different instances of the shape to be modeled. At this stage, only the adaptation part of the SONGWR algorithm is used. Adapting the network to a new instance is equivalent to using the model as a classifier: for each given point in the new shape instance, the best-matching node is selected (as the closest to the given input according to a pre-defined distance function) and adapted accordingly. The process has similarity with SOMs because there are no added/removed nodes anymore (note that the shape instances must be normalized before modeling; for more details on the method, see Ferrarini et al., 2005). After adapting the initial mesh to all other instances of the data set individually, every node of the initial mesh will have a corresponding cloud of matching nodes across the data set.

The aim of this work is to investigate local differences between two populations of shapes. It is therefore important that the models (*meshes*) used to describe the objects are sensitive to shape differences across individuals. In this respect, we followed the approach described in Davies et al. (2003) to evaluate the obtained mesh representation.

A mesh is composed of N nodes, where each node is characterized by three coordinates in the 3-dimensional space. Thus, each mesh is a $3 \times N$-dimensional object x in the feature space. Given a set of meshes, one can carry out a principal component analysis (PCA) to get a mean mesh and main eigen variations.

The performances of the resulting statistical model can be evaluated using the following functions:

$$C(M) = \sum_{m=1}^{M} p_m \tag{1}$$

$$E_r(M) = \frac{1}{N_S} \sum_{i=1}^{Ns} |S_i^{N_S}(M) - S_i| \tag{2}$$

$$G(M) = \frac{1}{N_S} \sum_{i=1}^{Ns} |S_i^{N_S-1}(M) - S_i| \tag{3}$$

$$S_p(M) = \frac{1}{N} \sum_{i=1}^{N} \mathrm{Diss}\left(S_i(M), \left\{S_1^T, \ldots, S_{N_S}^T\right\}\right) \tag{4}$$

$$\mathrm{Diss}\left(S_i(M), \left\{S_1^T, \ldots, S_{N_S}^T\right\}\right) = \frac{1}{N_S} \sum_{i=1}^{Ns} |S_i^T - S_i(M)| \tag{5}$$

where:

- Compactness $C(M)$: the percentage of variance in the data set that is covered by the first M modes of variation (where P_m is the percentage of total variation covered by the m^{th} mode). A better model requires a smaller number of modes to cover the same amount of variance.
- Reconstruction error $Er(M)$: the average accuracy in approximating the Ns shapes of the training set using M modes. S_i is the original shape whereas $S_i^{N_S}(M)$ is its approximation through a model based on all the N_s shapes. This function shows how

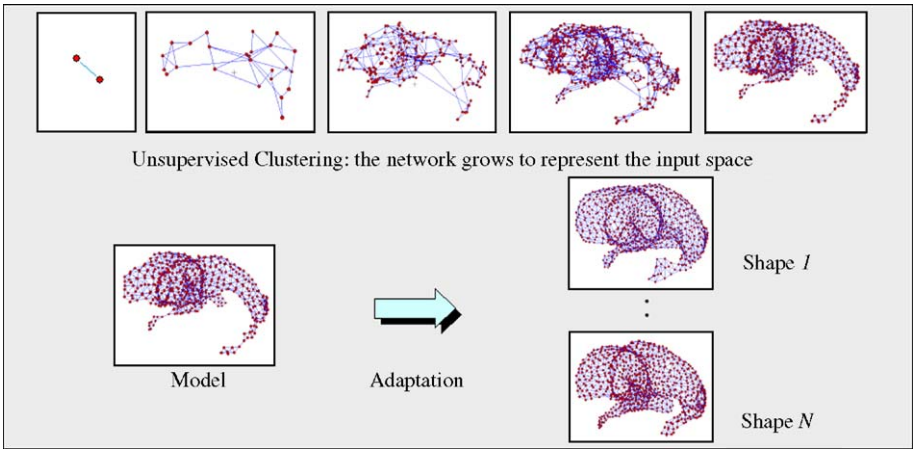

Fig. 2. The shape modeling algorithm: unsupervised surface point clustering and adaptation phase.

good the model is in reconstructing the shapes seen in the training set.

- Generalization error $G(M)$: for a given i, the shape S_i is approximated by a model generated with all the other shapes. The approximation is indicated as $S_i^{N_S-1}(M)$; this function shows how good the model is in generalizing what it has learnt from a training set, working on an unseen shape.
- Specificity error $S_p(M)$ is evaluated by uniformly sampling $N = 100$ instances $S_i(M)$ of the object class according to the model, and averaging the dissimilarity between them and the shapes in the training set S_i^T. This function shows how similar to the training set are the shapes one can create through the model.

There are mainly two factors that can strongly influence the performances of the final statistical model: the choice of the first shape-instance to be used to build the first mesh representation (Davies et al., 2002), and the accuracy threshold a_T (Marsland et al., 2002) that defines how accurate the first model should be in approximating the corresponding object. In this study, we have experimented with these two factors and chosen the best statistical model according to Eqs. (1)–(5).

The PCA approach described in this section is used mainly to identify global variations within each population and to estimate the performances with which the growing and adapting phases model the given shapes. An independent component analysis (ICA) approach could be used to highlight local variations within a population (Üzümcü et al., 2003), but this lies outside the scope of this work.

Surface-based statistical comparison

The highlighting of local shape difference between populations is possible because each node in the first model is uniquely labeled; it is thus possible to "follow" the node position when adapting to match (find) corresponding points within each population and across populations.

When comparing two populations, several statistical tests can be used. Permutation tests have been successfully applied to the analysis of brain images as in (Nichols and Holmes, 2001; Thompson et al., 2004); they require limited assumptions and provide correct results for multitest analysis when local information is needed (i.e., local surface comparison of two or more groups).

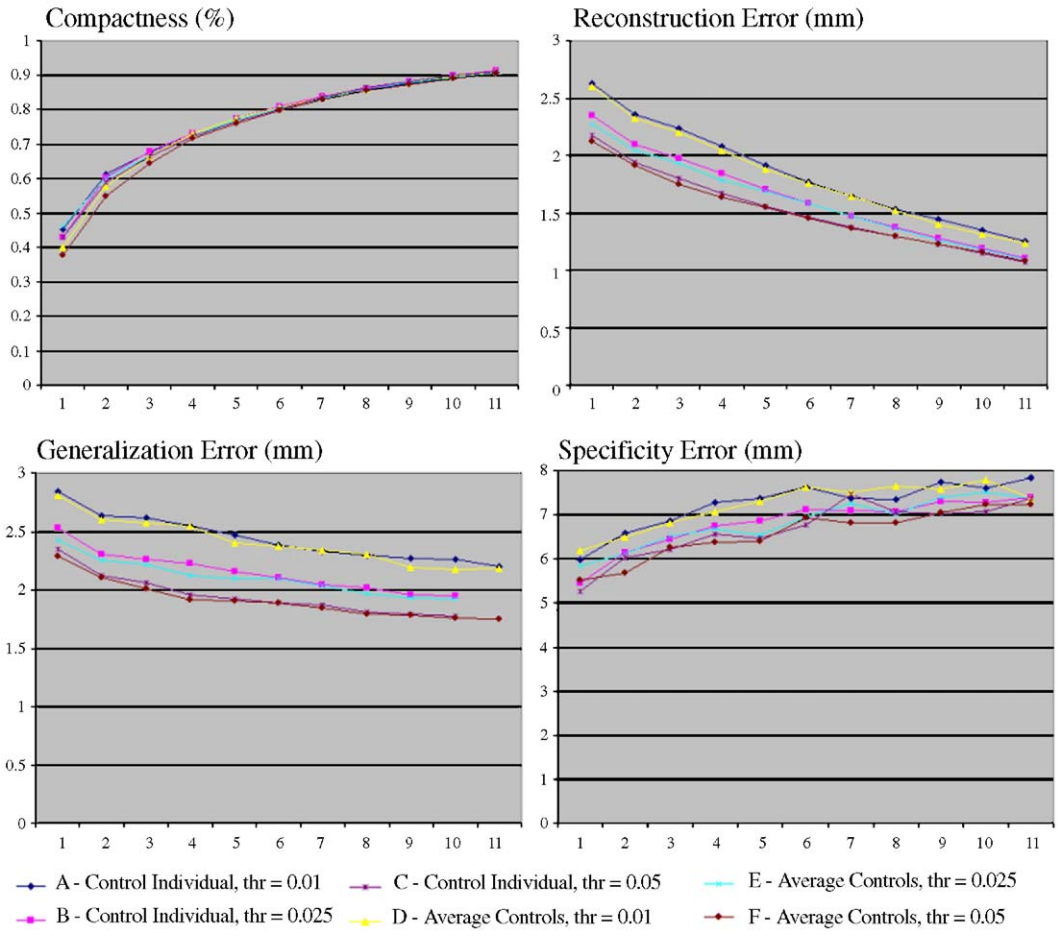

Fig. 3. PCA performances for statistical modeling of the ventricular shapes in the control group. The plots show how the performances change depending on the total number of modes of variation being considered (horizontal axis). Increasing the accuracy from 0.025 to 0.05 does not improve the model significantly. Using an average shape is generally better than using a good representative from the data set.

The problem can be formulated as follows: given two populations G_1 and G_2, are the shapes in G_1 significantly different from those in G_2? If the answer is positive, can we localize the difference on the average surface? In terms of feature space, the first question can be reformulated as "are G_1 and G_2 separable in the feature space?", whereas the second question seeks for features which mostly differentiate the two populations.

The outcome of the permutation tests is, in the first place, a P value for the omnibus hypothesis, "the two groups G_1 and G_2 are drawn from the same population". Moreover, we obtain the P values for each node in the model, showing whether the distribution of that node in space is the same in G_1 and G_2 or not. Permutation tests can be summarized as follows:

1. Considering two groups G_1 and G_2:
   i. Each node in the average model has two corresponding clouds of points C_1 and C_2, obtained considering the positions the corresponding nodes assume through all the shapes in G_1 and G_2.
   ii. C_1 and C_2 are compared via a Hotelling's T2 statistical test; the outcome of the test is the t value for the node comparison (are the node positions distributed in C_1 and C_2 in significantly different ways?).
2. For 10,000 times, two groups of shapes A and B are built up by randomly mixing G_1 and G_2, and point 1 is performed on them. Only the highest t value is stored for each iteration.
3. A critical t value t_c is evaluated as the k^{th} highest value of all the 10,000 t values previously stored (plus the $t_{\max}$ for the original subdivision in G_1–G_2), where

$$k = [\alpha * 10,000] + 1, \alpha = 0.05. \tag{6}$$

4. The P value for the omnibus hypothesis "G_1 and G_2 are the same" is evaluated as

$$P_{\text{value}} = \frac{N}{N_{\text{tests}}}, \text{where} \tag{7}$$

$$N = \{\text{stored } t_{\text{values}} / t_{\text{value}} > t_c\}, \tag{8}$$

$$N_{\text{tests}} = 10,000 + 1. \tag{9}$$

5. Finally, point 4 is applied to each single node, counting how many t values are higher than the t value associated with a particular node in the original G_1–G_2 grouping of

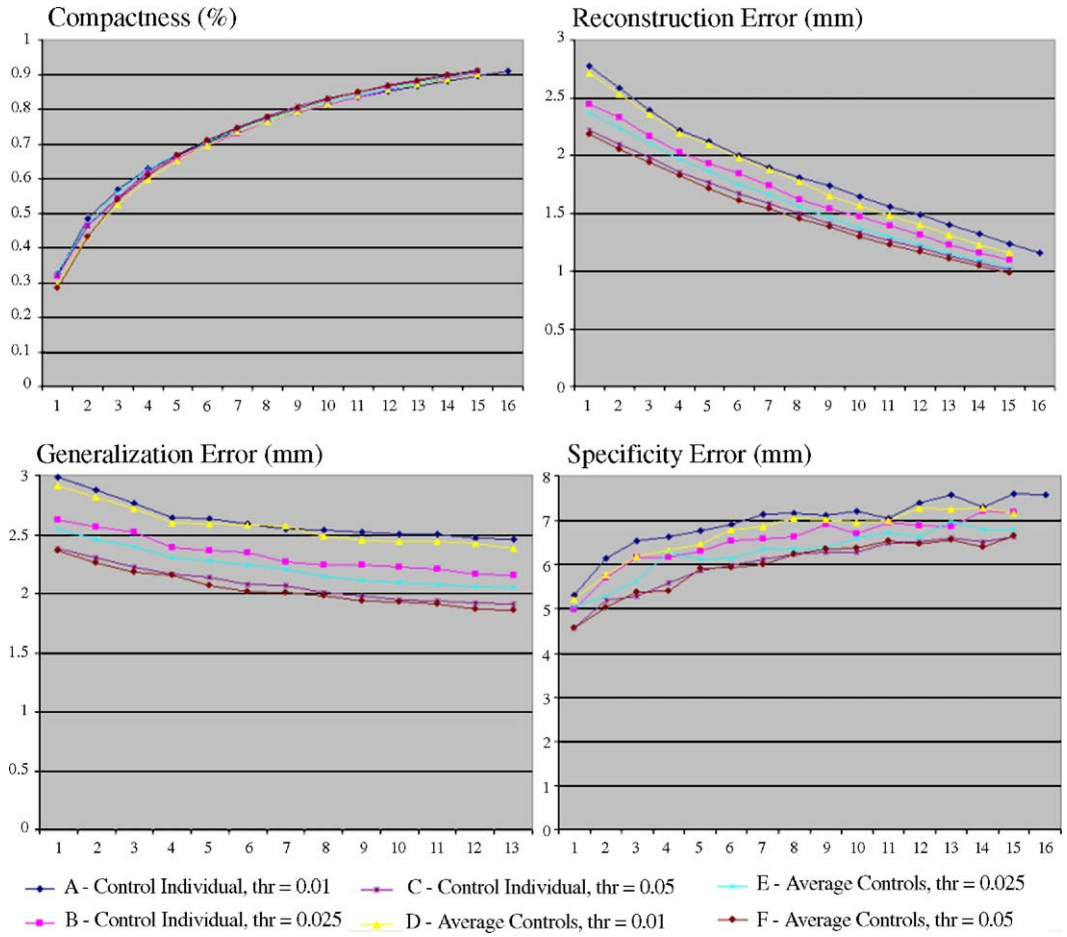

Fig. 4. PCA performances for statistical modeling of the ventricular shapes in the Alzheimer's disease group. The plots show how the performances change depending on the total number of modes of variation being considered (horizontal axis). The results are comparable to the modeling of the control group shown in Fig. 3.

Table 1
Computation load for different thresholds: we report the number of nodes of the final model and the time needed to adapt the model to a new shape

	No. of nodes	Adaptation time (in minutes, for shape)
$a_T = 0.01$	337	2 ± 1
$a_T = 0.025$	844	6 ± 2
$a_T = 0.05$	1689	16 ± 4

shapes, and dividing the number for 10000 + 1; this leads to a P value (corrected for multitests) for each node in the model.

Results

Optimal shape modeling parameters

In order to find the most suitable statistical model, we experimented with different threshold a_T and different initial shapes. As threshold level, we compared 0.01, 0.025, and 0.05. Concerning the initial shape, we considered a single case randomly selected out of the control population, and the average ventricle of the control population.

Results for compactness, reconstruction error, generalization error, and specificity error, obtained for the modeling of the ventricular shapes of the control group, are shown in Fig. 3. Those obtained for the AD group are given in Fig. 4. Table 1 shows the number of nodes and an indication of the adaptation

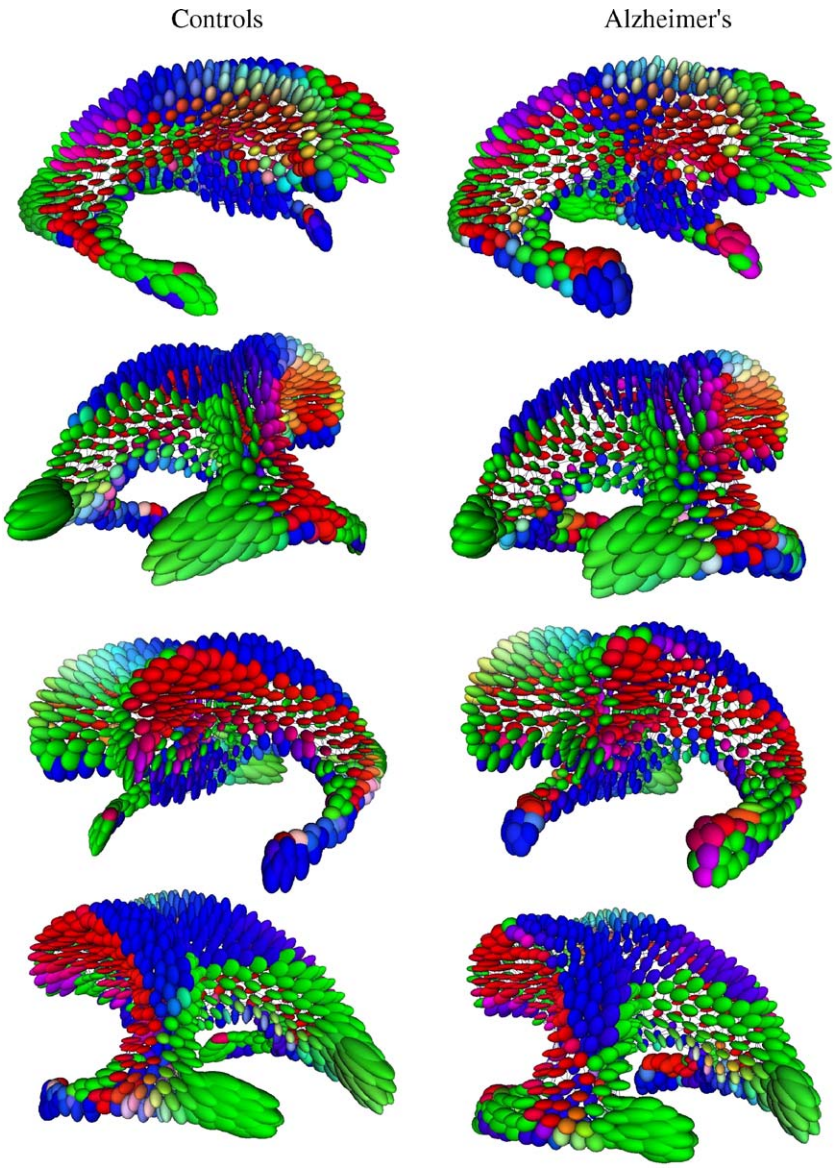

Fig. 5. Tensor-based representation of the nodes within control population (left column) and AD patients (right column). Each tensor is color-coded according to the direction of the main eigenvector: green for the inferior–posterior direction, blue for the inferior–anterior direction, and red for the left–right direction. (For interpretation of the references to colour in this figure legend, the reader is referred to the web version of this article.)

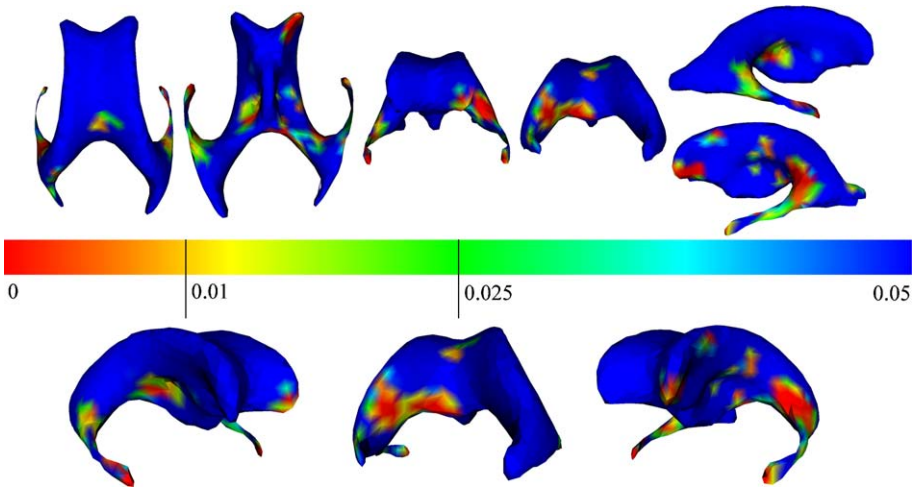

Fig. 6. Color-coded maps showing the P value associated with each node while comparing controls and AD patients. The P values were evaluated at $\alpha = 0.05$. (For interpretation of the references to colour in this figure legend, the reader is referred to the web version of this article.)

time for different thresholds (average of controls used as initial shape).

The use of an average initial shape gives slightly better results than an individual initial shape, when using the same threshold value a_T. Moreover, increasing the accuracy improves the final performances. The difference between average- and individual-initial shape was not pronounced, indicating that, in this application, the algorithm is moderately sensitive to this choice. With respect to the accuracy threshold, $a_T = 0.025$ and $a_T = 0.05$ gave significantly better results than $a_T = 0.01$, whereas the difference between 0.025 and 0.05 was not relevant. In order to keep a low computational load (see Table 1), we used $a_T = 0.025$, in combination with an average initial shape, for the rest of the experiments.

Tensor maps for group representation of global and local variations

Given a node in the model, we considered the cloud of locations the node assumed moving through matched nodes in the population: computing the covariance matrix associated with the cloud and its eigenvectors allows us to generate a tensor representation of the node. Fig. 5 shows the tensor representation of the model. Each ellipsoid represents the distribution in space of a particular node while moving across individuals belonging to the same group. The size of the ellipsoids is proportional to the eigenvalues of the tensor, whereas the color-coding maps the direction in space of the main eigenvector.

Most of the tensors present a first (main) mode of variation perpendicular to the surface rather than along the surface. Variations along the surface are generally a consequence of misplacement in adaptation (i.e., corresponding nodes that do not represent similar anatomical locations) or registration errors (i.e., small errors due to incorrect transformation matrix). Perpendicular variations are more likely to reflect real variations in shape because the nodes are always forced to be on the surface. Intuitively, the more perpendicular to the surface the tensor is, the better the node can capture the variations within a population and across populations. One can notice that the main modes of variation in both groups are the global dilation/shrinking of the ventricles and the elongation/contraction of the temporal horns.

The most striking results are the asymmetrical variations (left vs. right) between the inferior temporal horns within healthy controls as well as in the AD group. Note that in the control group, the left inferior horn presents mainly inferior–anterior thickening variations (blue) whereas the right inferior horn shows elongation variations in the inferior–posterior direction (green).

Both left and right horns are showing more pronounced variations (according to the sizes of the ellipsoids) within the AD group compared to the controls. In AD, the variations are also asymmetrical but different from those seen in controls: the right inferior horn is showing inferior–anterior widening (blue) whereas the left horn is showing mainly an enlargement in all directions; the tensors are almost isotropic (spherical). Because the color code is based on the value of the largest eigen value, there is a slight elongation tendency in the posterior–anterior direction (green) and a widening in left–right direction (red).

Statistical shape comparison of AD vs. controls using statistical maps

For each node, the P values derived from the permutation tests have been color-coded and mapped on an average model of the brain ventricles (see Fig. 6). Table 2 gives the percentage of area found to be significantly different at $\alpha = 0.05$ and $\alpha = 0.01$. Fig. 6 shows significant differences on the inferior lateral horns (left and right) and the areas adjacent to the left side of the splenium of the

Table 2
Number of nodes in the model and percentage of surface area found to be significantly different at 95% and 99% of confidence interval

	No. of nodes	% Total area	No. of node in left ventricles	% Left ventricle	No. of node in right ventricles	% Right ventricle
$\alpha = 0.05$	183	22	121	14	62	7
$\alpha = 0.01$	80	9	55	7	25	3

All the percentages are in respect to the total surface area of the brain ventricles.

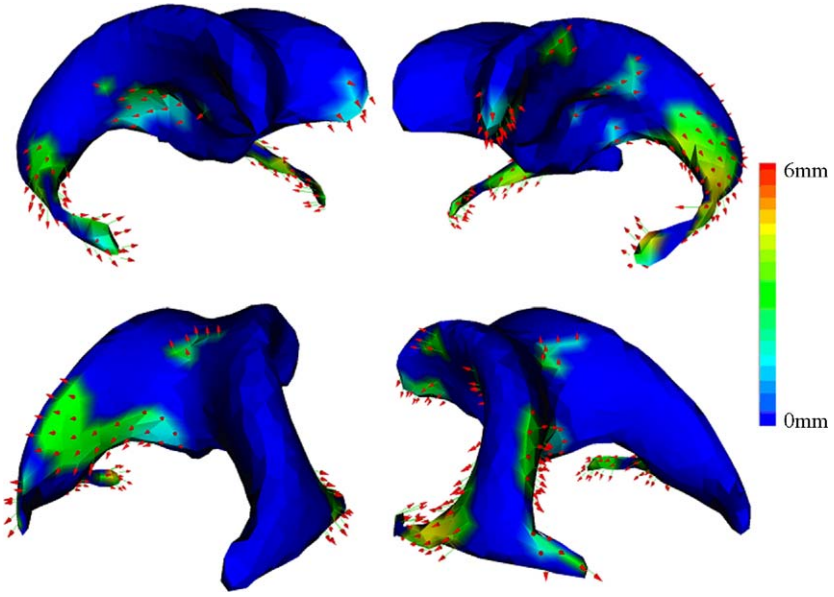

Fig. 7. Local changes required to transform an average control shape into an average AD shape. The direction of movement is indicated by the arrows; the amplitude of movement is color coded. (For interpretation of the references to colour in this figure legend, the reader is referred to the web version of this article.)

corpus callosum, a midsagittal area of the corpus callosum, the amygdala (left and right), the tale of the caudate nuclei (especially the left one), the head of the left caudate nucleus, and some areas adjacent to the thalamus (on the third ventricle).

A total area covering 22% of brain ventricular surface was significantly different with $P < 0.05$ and 9% of total brain ventricles presented significance at $P < 0.01$. The left lateral ventricle presented more significant differences (14% of the total surface at $P < 0.05$) as compared to the right ventricle (7%, $P < 0.05$).

Local shape comparison using displacement maps

Once the local area presenting the most significant local shape differences were identified, we computed the displacement vectors that would move a node from an average control shape to an average AD shape. Fig. 7 shows the direction of the displacement vectors for the significantly different nodes ($P < 0.05$). The length of the vectors is color-coded and mapped on the surface. In Fig. 8, we show both the main direction of normal variations (derived from the control group) and the directions of the control-to-Alzheimer transformation of Fig. 7. For most nodes, the direction control to Alzheimer is clearly not along (parallel) the normal variations (in control group); this confirms the significance of the local shape differences.

Discussion

The hippocampus and the corpus callosum are frequently studied structures in AD (Gootjes et al., 2006; Morys et al., 2002; Pol et al., 2005; Schott et al., 2005; Teipel et al., 2002; Adachi et

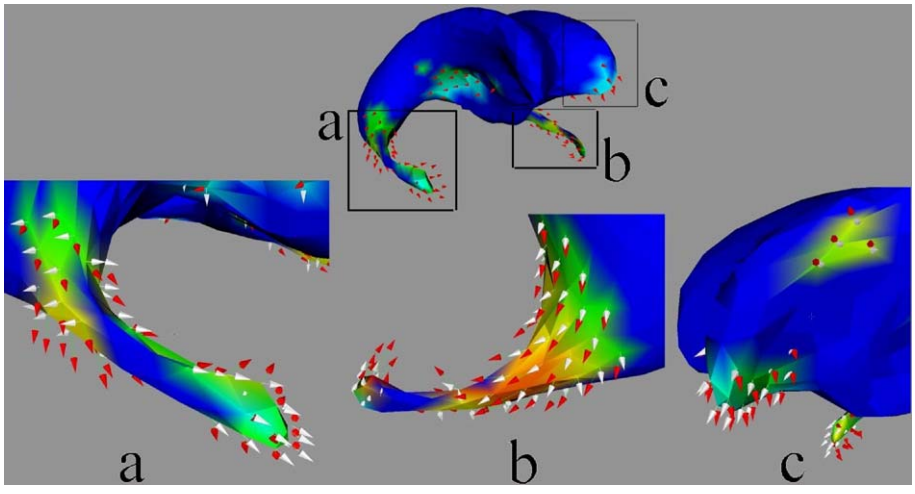

Fig. 8. Local changes required to transform an average control shape into an average AD shape (red arrows) compared with the main direction of variation within controls (white arrows). The images show the right and left temporal horns (left and middle images, respectively) and the frontal part of the left lateral ventricle (right image). Note that the arrows are not parallel, indicating different shape changes between the two groups. (For interpretation of the references to colour in this figure legend, the reader is referred to the web version of this article.)

al., 2003; Kantarci and Jack, 2003; Kodama et al., 2002; Petrella et al., 2003; Bracco et al., 1999; Gosche et al., 2001; Kaneko et al., 2004). Some other structures such as the lateral ventricular horn have also attracted the attention of researchers (Bracco et al., 1999; Frisoni et al., 2002; Thompson et al., 2004). Thompson et al. (2004) presented a longitudinal study to analyze the hippocampal and ventricular changes in AD. An anatomical surface modeling approach was combined with surface-based statistics to visualize the regions of significant shape differences between the two groups at both base line and follow-up scans as well as rate of atrophy in the serial MRI scans. They concluded that although both temporal horns and hippocampus maps correlated with clinical deterioration, temporal horn expansion maps were more sensitive to AD progression. In this paper, we extended the cross-sectional part of the analysis to the whole cerebral ventricular system (with the exception of the 4th ventricle) motivated by the fact that many adjacent brain structures are affected by dementia in general and AD in particular. Any change of shape and/or volume of the surrounding structure is directly reflected in the shape and volume of the ventricles.

Segmenting brain structures, such as the hippocampus, is tedious, time consuming, and often imprecise because most of these structures are relatively small and often do not present sufficient contrast or sharp borders. Furthermore, the white/gray matter image contrast in the elderly is considerably reduced as compared to young individuals, making any delineation (automatic or manual) a quite difficult and unreliable task. However, the contrast between CSF and the parenchyma remains sharp, thanks to clear CSF image intensity, irrespective of age. Therefore, the brain ventricle delineation is easier and more reliable.

Although the brain ventricles are relatively easy to delineate, their complex 3D shape is challenging to model and analyze. In this paper, we applied a fully automatic technique that is based on growing neural networks (Ferrarini et al., 2005). A first mesh model is generated on the average brain ventricles of the control group using the unsupervised growing phase of the algorithm. After convergence, the shape is adapted to every instance of the data set (healthy and AD subjects). The point correspondence is automatically established during the adaptation phase (automatic deformation) of the mesh.

We performed permutation tests for every node of the mesh and mapped the corresponding P values with a color code to highlight the local areas with significant differences (Fig. 6). For these areas, we computed the displacement vectors that would move a node from an average control shape to an average AD shape (Figs. 7 and 8).

Our results show that in patients with AD, not only the lateral horns were significantly affected by the disease, but also the areas adjacent to the anterior corpus callosum, the splenium of the corpus callosum, the amygdala, the thalamus, the tale of the caudate nuclei, and the head of the left caudate nucleus.

Although most of the analysis on brain morphology in AD are performed on high-resolution T1-weighted images, the MR images used in this work are quite standard in clinical settings (T2-weighted and FLAIR, 3 mm slice thickness). When scan time is not an issue, it is obviously preferable to acquire high-resolution images for morphology analysis. It would be therefore beneficial to run our experiments on higher resolution images and compare the extent of the areas showing significant differences. On the other hand, our work shows that even on relatively low-resolution images, shape differences can be picked up when studying the brain ventricles.

To our knowledge, this is the first study to report on local shape differences of the whole cerebral ventricular system in AD patients. The most widely used biomarker for AD is the volume of the hippocampus. However, the hippocampal atrophy occurs also in other dementias (van de Pol et al., 2006). In our preliminary study, we observed that apart from shape changes in the temporal horn, reflecting hippocampal atrophy, other brain parts of the ventricles also showed differences in shape when comparing AD patients and controls. Whether these additional ventricular shape changes permit superior differentiation of AD patients and patients with other neurodegenerative conditions should be subject to further research.

Acknowledgments

This work was supported by the Technology Foundation STW, applied science division of NWO and the technology program of the Ministry of Economic Affairs, and by Medis medical imaging systems, Leiden, The Netherlands (http://www.medis.nl).

References

Adachi, M., Kawakatsu, S., Hosoya, T., Otani, K., Honma, T., Shibata, A., Sugai, Y., 2003. Morphology of the inner structure of the hippocampal formation in Alzheimer disease. Am. J. Neuroradiol. 24 (8), 1575–1581.

Admiraal-Behloul, F., Heuvel, D.v.d., Olofsen, H., Schmitz, N., Buchem, M.A., 2003. Brain templates for the elderly. International Society for Magnetic Resonance in Medicine (ISMRM), Toronto.

Admiraal-Behloul, F., Heuvel, D.v.d., Olofsen, H., van Osch, M.J.P., van der Grond, J., van Buchem, M.A.R.J.H.C., 2005. Fully automatic segmentation of white matter hyperintensities in MR images of the elderly. NeuroImage 28 (3), 607–617.

Armstrong, C.L., Traipe, E., Hunter, J.V., Haselgrove, J.C., Ledakis, G.E., Tallent, E.M., Shera, D., Buchem, M.A., 2004. Age-related, regional, hemispheric, and medial–lateral differences in myelin integrity in vivo in the normal adult brain. Am. J. Neuroradiol. 25 (6), 977–984.

Barns, J., Scahill, R.I., Boyes, R.G., Frost, C., Lewis, E.B., Rossor, C.L., Rossor, M.N., Fox, N.C., 2004. Differentiating AD from aging using semiautomated measurement of hippocamapal atrophy rates. NeuroImage 23, 574–581.

Bozzao, A., Floris, R., Baviera, M.E., Apruzzese, A., Simonetti, G., 2001. Diffusion and perfusion MR imaging in cases of Alzheimer's disease: correlations with cortical atrophy and lesion load. Am. J. Neuroradiol. 22, 1030–1036.

Bracco, L., Piccini, C., Manfredi, G., Fonda, C., Falcini, M., Amaducci, L., 1999. Magnetic resonance measures in Alzheimer disease: their utility in early diagnosis and evaluating disease progression. Alzheimer Dis. Assoc. Disord. 13 (3), 157–164.

Bronge, L., Bogdanovic, N., Wahlumd, L.O., 2002. Postmortem MRI and histopathology of white matter changes in Alzheimer brains. A quantitative, comparative study. Dementia Geriatr. Cognit. Disord. 13, 205–212.

Coffey, C.E., Wilkinson, W.E., Parashos, I.A., 1992. Quantitative cerebral anatomy of aging human brain: a cross-sectional study using magnetic resonance imaging. Neurology 42, 527–536.

Cootes, T.F., Taylor, C.J., Cooper, D.H., Graham, J., 1995. Active shape models—Their training and application. Comput. Vis. Image Underst. 61 (1), 38–59.

Davies, R.H., Twining, C.J., Cootes, T.F., Waterton, J.C., Tayolr, C.J., 2002. A minimum description length approach to statistical shape modelling. IEEE Trans. Med. Imag. 21, 525–537.

Davies, R.H., Twining, C.J., Allen, P.D., Cootes, T.F., Taylor, C.J., 2003. Shape discrimination in the hippocampus using an MDL model. IPMI 38–50.

Dekaban, A.S., 1978. Changes in brain weights during the span of human life: relation of brain weights to body heights and body weights. Ann. Neurol. 4, 345–356.

Ferrarini, L., Olofsen, H., Buchem, M.A., Reiber, J.H.C., Admiraal-Behloul, F., 2005. Fully automatic shape modelling using growing cell neural networks. MICCAI Lect. Notes Comput. Sci. 3750, 451–458.

Freeborough, P.A., Fox, N.C., 1997. The boundary shift integral: an accurate and robust measure of cerebral volume changes from registered repeat MRI. IEEE Trans. Med. Imag. 16 (5), 623–629.

Frisoni, G.B., Geroldi, C., Beltramello, A., Bianchetti, A., Binetti, G., Bordiga, G., DeCarli, C., Laakso, M.P., Soininen, H., Testa, C., Zanetti, O., Trabucchi, M., 2002. Radial width of the temporal horn: a sensitive measure in Alzheimer disease. Am. J. Neuroradiol. 23 (1), 35–47.

Fritzke, B., 1992. Kohonen feature maps and growing cell structures—A performance comparison. NIPS 123–130.

Fritzke, B., 1994. Growing cell structures—A self-organizing network for unsupervised and supervised learning. Neural Netw. 7 (9), 1441–1460.

Gootjes, L., Bouma, A., Strien, J.W., Schijndel, R.v., Barkhof, F., Scheltens, P., 2006. Corpus callosum size correlates with asymmetric performance on a dichotic listening task in healthy aging but not in Alzheimer's disease. Neuropsychologia 44 (2), 208–217.

Gosche, K.M., Mortimer, J.A., Smith, C.D., Markesbery, W.R., Snowdon, D.A., 2001. An automated technique for measuring hippocampal volumes from MR imaging studies. Am. J. Neuroradiol. 22 (9), 1686–1689.

Hanyu, H., Asano, T., Sakurai, H., Imon, Y., Iwamoto, T., Takazaki, M., Shindo, H., Abe, K., 1999. Diffusion-weighted and magnetization transfer imaging of the corpus callosum in Alzheimer's disease: a quantitative study. J. Neurol. Sci. 167, 37–44.

Kaneko, T., Kodama, N., Kaeriyama, T., Kawase, Y., Shibukawa, M., Fukumoto, I., 2004. Automatic extraction of corpus callosum from midsagittal head MR image and examination of Alzheimer-type dementia objective diagnostic system in feature analysis. Nippon Hoshasen Gijutsu Gakkai Zasshi 60 (2), 293–298.

Kantarci, K., Jack Jr., C.R., 2003. Neuroimaging in Alzheimer disease: an evidence-based review. NeuroImaging Clin. N. Am. 13 (2), 197–209.

Kodama, N., Shimada, T., Fukumoto, I., 2002. Image-based diagnosis of Alzheimer-type dementia: measurements of hippocampal and ventricular areas in MR images. Magn. Reson. Med. Sci. 1 (1), 14–20.

Lerch, J.P., Pruessner, J.C., Zijdenbos, A., Hampel, H., Teipel, S.J., Evans, A.C., 2005. Focal decline of cortical thickness in Alzheimer's disease identified by computational neuroanatomy. Cereb. Cortex 15, 995–1001.

Marsland, S., Shapiro, J., Nehmzow, U., 2002. A self-organizing network that grows when required. Neural Netw. 15, 1041–1058.

Morys, J., Boek-Billewicz, B., Dziewiatkowaski, J., Bidzan, L., Ussorowska, D., Narklewicz, O., 2002. Changes in the volume of temporal lobe structures related to Alzheimer's type dementia. Folia Neuropathol. 40 (2), 47–56.

Nichols, T.E., Holmes, A.P., 2001. Nonparametric permutation tests for functional neuroimaging: a primer with examples. Hum. Brain Mapp. 15, 1–25.

Petrella, J.R., Coleman, R.E., Doraiswamy, P.M., 2003. Neuroimaging and early diagnosis of Alzheimer disease: a look to the future. Radiology 226 (2), 315–336.

Pitiot, A., Delingette, H., Toga, A.W., Thompson, P.M., 2003. Learning object correspondences with the observed transport shape measure. IPMI 25–37.

Pol, L.A., Hensel, A., Flier, W.M., Visser, P.J., Pijnenburg, Y.A., Barkhof, F., Gertz, H.J., Scheltens, P., 2005. Hippocampal atrophy on MRI in frontotemporal lobar degeneration and Alzheimer's disease. J. Neurol. Neurosurg. 23.

Pruessner, J.C., Collins, D.L., Pruessner, M., Evans, A.C., 2001. Age and gender predict volume decline in the anterior and posterior hippocampus in early adulthood. J. Neurosci. 21 (1), 194–200.

Raz, N., Gunning, F.M., Head, D., 1997. Selective aging of the human cerebral cortex observed in vivo: differential vulnerability of the prefrontal gray matter. Cereb. Cortex 7, 268–282.

Rueckert, D., Frangi, A.F., Schnabel, J.A., 2003. Automatic construction of 3-D statistical deformation models of the brain using nonrigid registration. IEEE Trans. Med. Imag. 22 (8), 1014–1025.

Scheltens, P., Barkhof, F., Lejs, D., Wolters, E.C., Ravid, R., Kamphorst, W., 1995. Histopathologic correlates of white matter changes on MRI in Alzheimer's disease and normal aging. Neurology 45 (5), 883–888.

Schott, J.M., Price, S.L., Frost, C., Whitwell, J.L., Rossor, M.N., Fox, N.C., 2005. Measuring atrophy in Alzheimer diseases: a serial MRI study over 6 and 12 months. Neurology 65, 119–124.

Showell, E.R., Peterson, B.S., Thompson, P.M., 2003. Mapping cortical changes across the human life span. Nat. Neurosci. 6, 309–315.

Spilt, A., Geeraedts, T., Craen, A.J., Westendorp, R.G., Blauw, G.J., Buchem, M.A., 2005. Age-related changes in normal-appearing brain tissue and white matter hyperintensities: more of the same or something else? Am. J. Neuroradiol. 26 (4), 725–729.

Teipel, S.J., Bayer, W., Alexander, G.E., Zebhuhr, Y., Teichberg, D., Kulic, L., Schapiro, M.B., Moller, H.J., Rapoport, S.I., Hampel, H., 2002. Progression of corpus callosum atrophy in Alzheimer disease. Arch. Neurol. 59, 243–248.

Thodberg, H.H., 2003. Minimum description length shape and appearance models. IPMI 51–62.

Thompson, P.M., Hayashi, K.M., Zubicary, G., 2003. Dynamics of gray matter loss in Alzheimer's disease. J. Neurosci. 23, 994–1005.

Thompson, P.M., Hayashi, K.M., Zubicaray, G.I., Janke, A.L., Rose, S.E., Semple, J., Hong, S., Herman, D.H., Gravano, D., Doddrell, D.M., Toga, A.W., 2004. Mapping hippocampal and ventricular change in Alzheimer disease. NeuroImage 22 (4), 1754–1766.

Üzümcü, M., Frangi, A.F., Reiber, J.H.C., Lelieveldt, B.P.F., 2003. Independent component analysis in statistical shape models. Proc. SPIE 5032, 375–383.

van de Pol, L.A., Hensel, A., van der Flier, W.M., Visser, P.J., Pijnenburg, Y.A., Barkhof, F., Gertz, H.J., Scheltens, P., 2006. Hippocampal atrophy on MRI in frontotemporal lobar degeneration and Alzheimer's disease. J. Neurol., Neurosurg. Psychiatry 77, 439–442.

Woods, R.P., Grafton, S.T., Holmes, C.J., Chery, S.R., Mazziotta, J.C., 1998. Automated image registration I. General methods and intrasubject, intramodality validation. J. Comput. Assist. Tomogr. 22, 139–152.